Fractal mechanism of basin of attraction in passive dynamic walking

AUTHOR(S):

Okamoto, Kota; Aoi, Shinya; Obayashi, Ippei; Kokubu, Hiroshi; Senda, Kei; Tsuchiya, Kazuo

CITATION:

Okamoto, Kota ...[et al]. Fractal mechanism of basin of attraction in passive dynamic walking. Bioinspiration & Biomimetics 2020, 15(5): 055002.

ISSUE DATE:

2020-09

URL:

http://hdl.handle.net/2433/254686

Bioinspiration & Biomimetics

PAPER • **OPEN ACCESS**

Fractal mechanism of basin of attraction in passive dynamic walking

To cite this article: Kota Okamoto *et al* 2020 *Bioinspir. Biomim.* **15** 055002

IOP Publishing *Bioinspir. Biomim.* **15** (2020) 055002 https://doi.org/10.1088/1748-3190/ab9283

Bioinspiration & Biomimetics

PAPER

Fractal mechanism of basin of attraction in passive dynamic walking

Kota Okamoto[1], **Shinya Aoi**[1,4], **Ippei Obayashi**[2], **Hiroshi Kokubu**[3], **Kei Senda**[1] and **Kazuo Tsuchiya**[1]

[1] Dept. of Aeronautics and Astronautics, Graduate School of Engineering, Kyoto University, Kyoto, Japan
[2] Center for Advanced Intelligence Project, RIKEN, Tokyo, Japan
[3] Dept. of Mathematics, Graduate School of Science, Kyoto University, Kyoto, Japan
[4] Author to whom any correspondence should be addressed.

E-mail: shinya_aoi@kuaero.kyoto-u.ac.jp

Keywords: passive dynamic walking, stability, basin of attraction, fractal

RECEIVED
4 March 2020

REVISED
24 April 2020

ACCEPTED FOR PUBLICATION
12 May 2020

PUBLISHED
6 July 2020

Abstract

Passive dynamic walking is a model that walks down a shallow slope without any control or input. This model has been widely used to investigate how humans walk with low energy consumption and provides design principles for energy-efficient biped robots. However, the basin of attraction is very small and thin and has a fractal-like complicated shape, which makes producing stable walking difficult. In our previous study, we used the simplest walking model and investigated the fractal-like basin of attraction based on dynamical systems theory by focusing on the hybrid dynamics of the model composed of the continuous dynamics with saddle hyperbolicity and the discontinuous dynamics caused by the impact upon foot contact. We clarified that the fractal-like basin of attraction is generated through iterative stretching and bending deformations of the domain of the Poincaré map by sequential inverse images. However, whether the fractal-like basin of attraction is actually fractal, i.e., whether infinitely many self-similar patterns are embedded in the basin of attraction, is dependent on the slope angle, and the mechanism remains unclear. In the present study, we improved our previous analysis in order to clarify this mechanism. In particular, we newly focused on the range of the Poincaré map and specified the regions that are stretched and bent by the sequential inverse images of the Poincaré map. Through the analysis of the specified regions, we clarified the conditions and mechanism required for the basin of attraction to be fractal.

1. Introduction

Passive dynamic walking is a model that walks down a shallow slope without any control or input [27], which is useful for investigating the mechanism of generating stable walking from a dynamic viewpoint. This has been widely used to examine how humans walk with low energy consumption [6, 7, 11, 24–26] and to provide design principles for energy-efficient biped robots [5, 9, 10, 21–23, 36, 37]. However, the basin of attraction is very small and thin and has a fractal-like complicated shape [2, 29, 33], which makes it difficult to produce stable walking. Furthermore, chaos appears in the walking behavior through a period-doubling cascade by increasing the slope angle [15], which makes producing stable walking even more difficult. Meanwhile, the basin of attraction shows a fractal-like shape, even without period doubling. In other words, the fractal-like basin of attraction appears even for a single attractor. Although this indicates that a different mechanism from the period doubling of the attractor induces a fractal-like basin of attraction, the mechanism is unclear.

In our previous study [29], we used the simplest walking model [13] for the analysis of passive dynamic walking and clarified the formation mechanism for the basin of attraction based on dynamical systems theory by focusing on the hybrid dynamics of the model composed of the continuous dynamics generated by the equations of motion during the swing phase with saddle hyperbolicity and the discontinuous dynamics generated by the impact upon foot contact. Specifically, we found that the fractal-like basin of attraction is generated through iterative stretching and bending deformations by sequential inverse images of the Poincaré map for the collection of initial conditions from which the model can walk

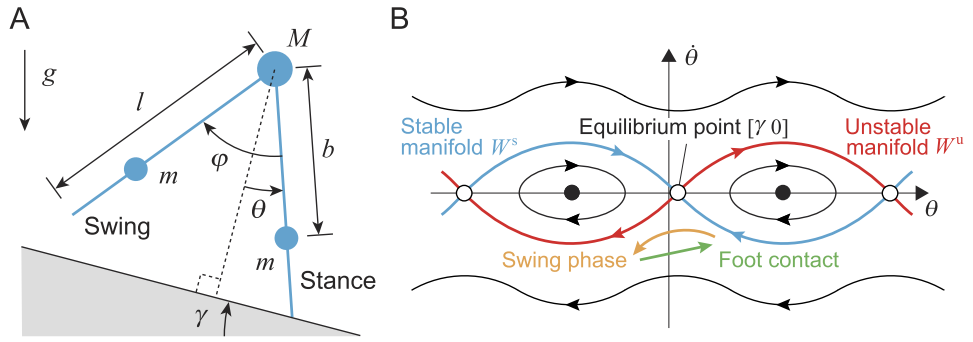

Figure 1. Passive dynamic walking. (A) Compass-type model. (B) Phase diagram $[\theta\,\dot{\theta}]$. Equilibrium point $[\theta\,\dot{\theta}] = [\gamma\,0]$ is a saddle point. Stable walking (indicated by the two arrows below the equilibrium point) is obtained by the continuous dynamics during the swing phase and the discontinuous dynamics upon foot contact.

at least one step, which corresponds to the domain of the Poincaré map. However, whether the fractal-like basin of attraction is actually fractal, i.e., whether infinitely many self-similar patterns are embedded in the basin of attraction, is dependent on the model parameters, such as the slope angle [2, 33]. The mechanism that determines whether the basin of attraction is fractal remains unclear.

In the present study, we improved our previous analysis in order to clarify the mechanism. In particular, we newly focused on the range of the Poincaré map, which corresponds to the collection of states after the model walked one step starting from the domain, and specified the regions that are stretched and bent by the sequential inverse image of the Poincaré map. Through analysis of the specified regions, we clarified the condition and mechanism required for the basin of attraction to be fractal.

2. Method

2.1. Model

In the present study, we used a compass-type model (figure 1(A)) for the analysis of passive dynamic walking. This model has two legs (rigid links), the lengths of which are both l, connected by a frictionless hip joint. Here, θ is the angle of the stance leg with respect to the slope normal, and φ is the relative angle between the stance and swing legs. The mass is located only at the hip and the leg. The hip mass is M, and the leg mass is m. The leg mass is located at a distance b from the hip joint. In addition, g is the acceleration due to gravity. This model walks on a slope of angle γ without any control or input.

2.2. Structure of phase space by hybrid dynamics

In the present study, we focused on the simplest walking model, where $m/M \to 0$ and $b/l \to 1$ [13], because the dynamical characteristics remain almost unchanged [29]. This model is governed by hybrid dynamics composed of the continuous dynamics generated by the equations of motion during the swing phase and the discontinuous dynamics generated by the impact upon foot contact.

The equations of motion are given by

$$\ddot{\theta} - \sin(\theta - \gamma) = 0 \tag{1}$$

$$(\cos\varphi - 1)\ddot{\theta} + \ddot{\varphi} - \dot{\theta}^2 \sin\varphi + \sin(\varphi - \theta + \gamma) = 0 \tag{2}$$

These equations are nondimensionalized by the time scale $\sqrt{l/g}$ and have an equilibrium point $[\theta\,\dot{\theta}\,\varphi\,\dot{\varphi}] = [\gamma\,0\,0\,0]$, which describes the situation where both legs are upright. The eigenvalues of the linearized equations of motion at the equilibrium point are ± 1 and $\pm i$, and the equilibrium point is a saddle center with one stable direction, one unstable direction, and two neutral directions. Specifically, θ is determined only by (1) and is not affected by φ. This equation for θ has a saddle equilibrium point at $[\theta\,\dot{\theta}] = [\gamma\,0]$, as shown in figure 1(B). In the phase diagram of $[\theta\,\dot{\theta}]$ the trajectories going into and out of the equilibrium point are the stable manifold W^{s} and the unstable manifold W^{u}, respectively. In the phase space of four variables $[\theta\,\dot{\theta}\,\varphi\,\dot{\varphi}]$, $W^{\mathrm{s}} \times \mathbb{R}^2$ and $W^{\mathrm{u}} \times \mathbb{R}^2$ are the center-stable manifold and the center-unstable manifold, respectively, and we denote them by W^{cs} and W^{cu}.

Foot contact occurs when the following conditions are satisfied:

$$2\theta - \varphi = 0 \tag{3}$$

$$-\pi/2 < \theta < 0 \tag{4}$$

$$2\dot{\theta} - \dot{\varphi} < 0 \tag{5}$$

The impact upon foot contact yields the following relationship:

$$\begin{bmatrix} \theta^+ \\ \dot{\theta}^+ \\ \varphi^+ \\ \dot{\varphi}^+ \end{bmatrix} = \begin{bmatrix} -\theta^- \\ \dot{\theta}^- \cos 2\theta^- \\ -2\theta^- \\ \cos 2\theta^- (1 - \cos 2\theta^-)\dot{\theta}^- \end{bmatrix} \tag{6}$$

where $*^-$ and $*^+$ are the state $*$ just before and after the foot contact, respectively. The important property of this relationship is that the state just

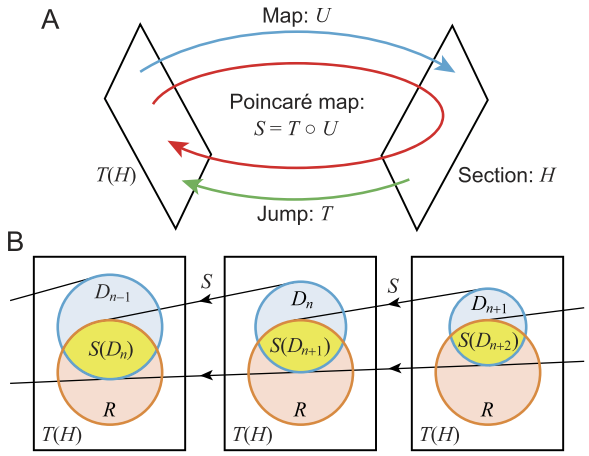

Figure 2. Schematic diagram of the structure of the phase space. (A) Hybrid dynamics composed of the section H, jump T, and map U. (B) Relationship among D_n, $S(D_n)$, and R on $T(H)$.

after foot contact $[\theta^+ \dot{\theta}^+ \varphi^+ \dot{\varphi}^+]$ depends only on $[\theta^- \dot{\theta}^-]$ and is independent of $[\varphi^- \dot{\varphi}^-]$. This means that the state just after foot contact forms a two-dimensional surface in the four-dimensional phase space $[\theta^- \dot{\theta}^- \varphi^- \dot{\varphi}^-]$ and satisfies the following two conditions:

$$2\theta^+ = \varphi^+ \tag{7}$$

$$\dot{\varphi}^+ = \dot{\theta}^+(1 - \cos 2\theta^+) \tag{8}$$

In addition, from (4), the state just after foot contact also satisfies

$$0 < \theta^+ < \pi/2 \tag{9}$$

However, note that since the state just after foot contact is independent of $\dot{\varphi}^-$, (5) generates no condition.

This hybrid dynamic system determines the structure of the phase space, as shown in figure 2(A). Here, H is the section defined by the foot contact conditions (3)–(5) and forms a three-dimensional space in the four-dimensional phase space, and T is the jump in the phase space from the state just before foot contact to the state just after foot contact, as defined by (6). Therefore, the image of T, $T(H)$, is the region representing all states just after foot contact, and a new step starts from $T(H)$. Moreover, U is the map from the start of a step to the next instance of foot contact. In other words, U is the map from $T(H)$ to H, as defined by the equations of motion (1) and (2). The Poincaré map S is defined on the Poincaré section $T(H)$ by

$$S = T \circ U : T(H) \to T(H) \tag{10}$$

This Poincaré map S represents one step, and an attractor of S represents stable walking. The basin of attraction of S is the main topic of the present paper. Here, S is parameterized by one parameter γ. In particular, S has an attracting fixed point at $0 < \gamma < 0.015$, and there is a period-doubling cascade to chaos for $0.015 < \gamma < 0.019$ [13].

2.3. Domain of Poincaré map and basin of attraction

We define $D_n (n = 1, 2, \ldots)$ as the collection of initial conditions on $T(H)$ from which the model walks at least n steps. This satisfies $D_{n+1} \subseteq D_n$ (figure 2(B)), which means that when the initial condition is in D_n but out of D_{n+1}, the model will fall down at the $n+1$th step. Since the Poincaré map S represents walking one step, $S(D_n)$ indicates the state on $T(H)$ after the model walked one step starting from D_n. Since the model can walk at least $n-1$ steps from $S(D_n)$, the following condition is satisfied:

$$S(D_n) \subseteq D_{n-1} \tag{11}$$

Since the domain D of S on $T(H)$ represents the collection of initial conditions on $T(H)$ from which the model walks at least one step, D is identical to D_1.

Using the inverse image of S, we can write $D_n = S^{-1}(D_{n-1})$. However, S^{-1} acts only on a part of D_{n-1}, as shown in figure 2(B), as clarified in the following section. First, the range R of S on $T(H)$ is given by $R = S(D_1)$ because D_1 is the domain of S, which corresponds to the collection of states after the model successfully walked one step starting from all states on $T(H)$. This means that the state after each step must be in R unless the model falls down. The following equation is satisfied:

$$S(D_n) = D_{n-1} \cap R \tag{12}$$

We prove this below. First, since $D_n \subseteq D_1$, $S(D_n) \subseteq R$. Based on this consideration and (11), $S(D_n) \subseteq D_{n-1} \cap R$. Second, we assume that $d \nsubseteq S(D_n)$ for $\exists d \subseteq D_{n-1} \cap R$. Since d is in R, S^{-1} is applicable to d, and, since d is in D_{n-1}, $S^{-1}(d) \subseteq D_n$. This contradicts $d \nsubseteq S(D_n)$. Therefore, this assumption is not satisfied. Since any state in $D_{n-1} \cap R$ is in $S(D_n)$, we obtain (12). Therefore, instead of $D_n = S^{-1}(D_{n-1})$, we use

$$D_n = S^{-1}(D_{n-1} \cap R) \tag{13}$$

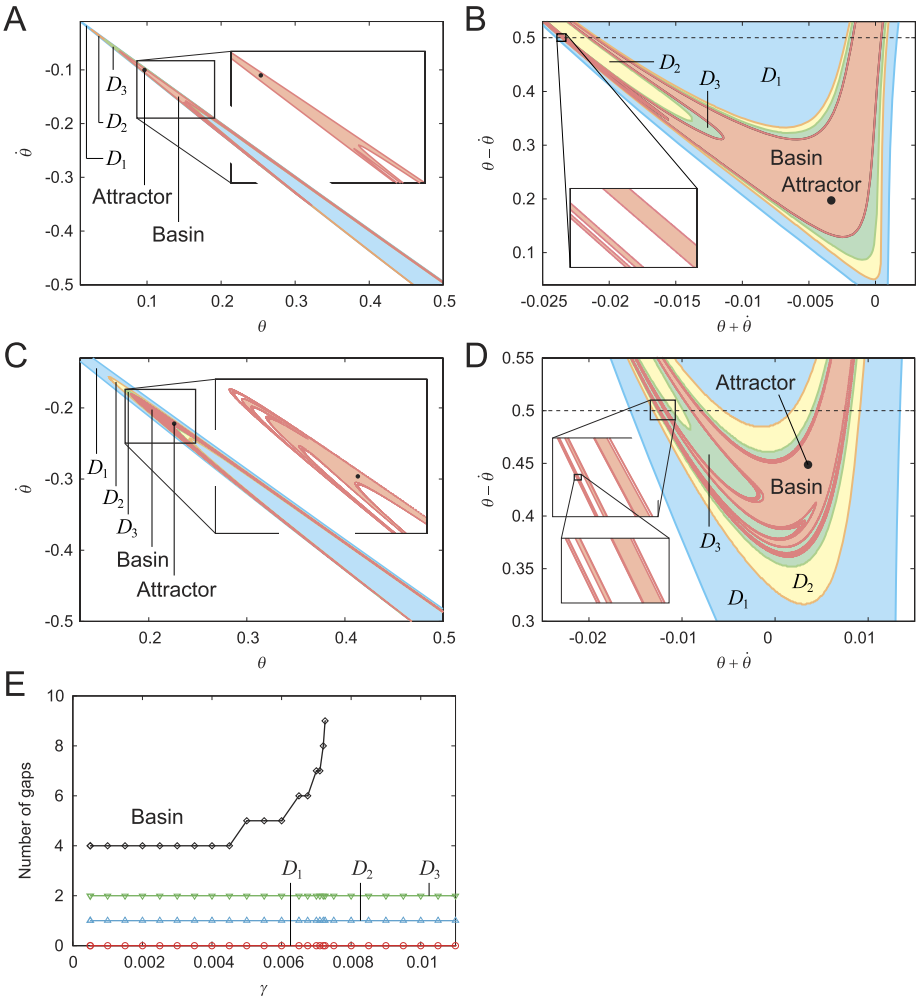

Figure 3. Evolution of the basin of attraction through D_1, D_2, and D_3. (A)–(D) D_1, D_2, D_3, and the basin of attraction for $\gamma = 0.001$ (A) and (B) and 0.013 (C) and (D) in the θ-$\dot{\theta}$ plane and $(\theta+\dot{\theta})$-$(\theta-\dot{\theta})$ plane, respectively. Parts of the basin of attraction are enlarged. (E) The number of gaps on $\theta-\dot{\theta}=0.5$ depending on γ.

In the same manner, instead of $D_n = S^{-n+1}(D_1)$, we use

$$D_n = S^{-1}\left(S^{-1}\left(\ldots\left(S^{-1}\left(D_1 \cap R\right)\cap R\right)\ldots\cap R\right)\cap R\right) \tag{14}$$

Since the model walks at least n steps from D_n, D_n approximates the basin of attraction as n increases. We confirmed the convergence by comparing D_{100} and D_{200} using $10^4 \times 10^4$ initial states.

3. Results

3.1. D_n and basin of attraction

Figures 3(A) and (C) show D_1, D_2, D_3, and the basin of attraction for $\gamma = 0.001$ and 0.013, respectively. In order to clarify these geometric characteristics, we used $\theta+\dot{\theta}$ and $\theta-\dot{\theta}$ for the axes for $\gamma = 0.001$ and 0.013 in figures 3(B) and (D), respectively, as in our previous study [29]. Here, D_2 and D_3 are V-shaped, and D_3 has a thin slit (note that a V-shaped region indicates that the basin has one large slit). The basins of attraction have multiple slits and are complicated. In particular, while the basin of attraction has only a few slits for $\gamma = 0.001$, the basin has a number of slits, and self-similar patterns are embedded for $\gamma = 0.013$. In order to quantitatively clarify these properties, we examined how many gaps D_1, D_2, D_3, and the basin of attraction have on the line $\theta-\dot{\theta}=0.5$. As a result, there are zero, one, two, and four gaps in D_1, D_2, D_3, and the basin of attraction, respectively, for $\gamma = 0.001$. In contrast, there are zero, one, two, and infinitely many gaps in D_1, D_2, D_3, and the basin of attraction, respectively, for $\gamma = 0.013$. We further investigated the number of slits in D_1, D_2, D_3, and the basin of attraction for γ based on the gaps on $\theta-\dot{\theta}=0.5$ in figure 3(E). The number of slits in D_n increases as n increases, and that in the basin of attraction increases exponentially as γ increases. Fractal structures appear in the basin of attraction over $\gamma \approx 0.0075$.

3.2. $D_1 \cap R$

Since $D_n = S^{-1}(S^{-1}(\ldots(S^{-1}(D_1 \cap R)\cap R)\ldots\cap R)\cap R)$ approximates the basin of attraction as $n\to\infty$, we begin with $D_1 \cap R$ to investigate the formation mechanism of the basin of attraction. As shown in

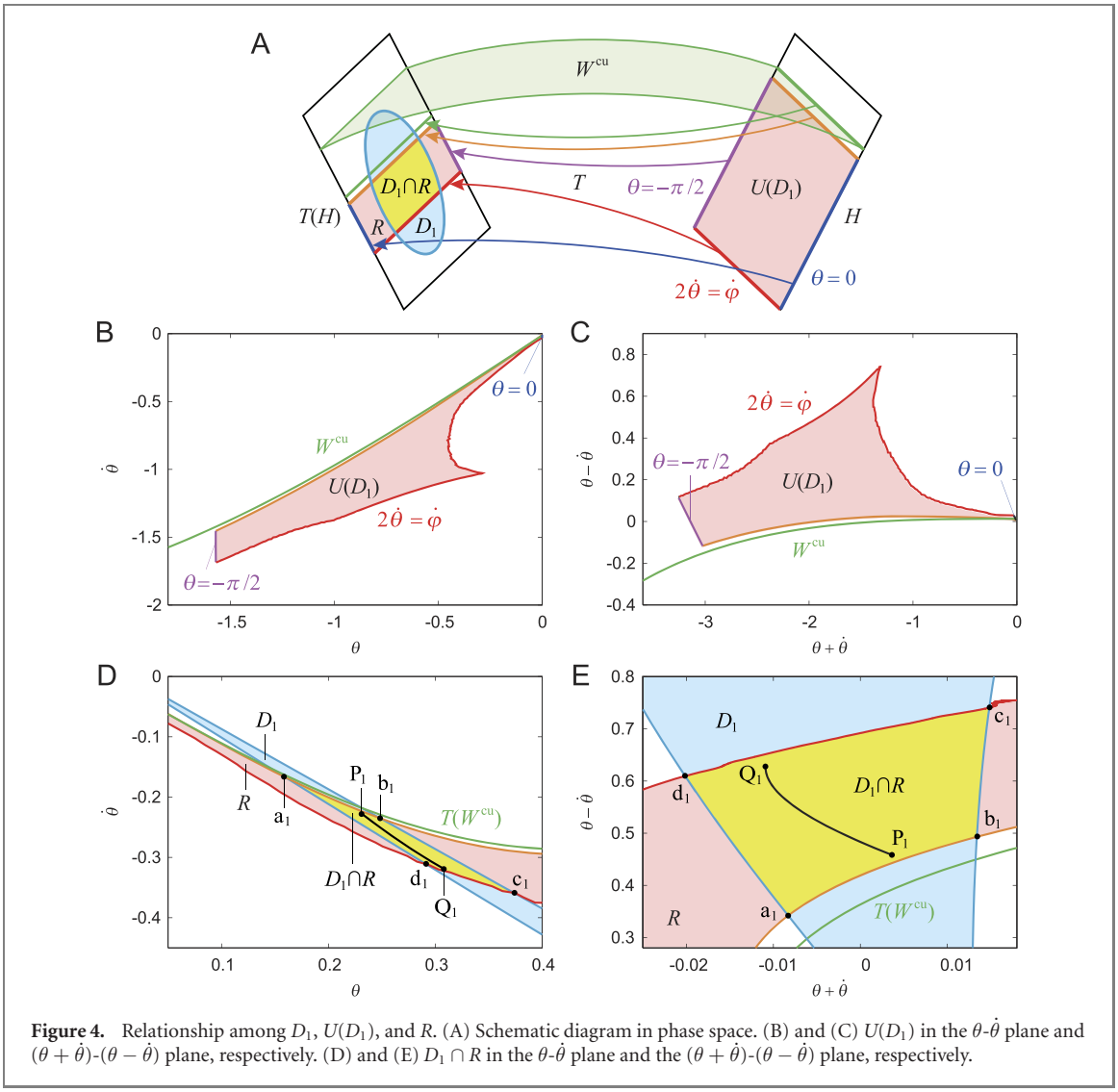

Figure 4. Relationship among D_1, $U(D_1)$, and R. (A) Schematic diagram in phase space. (B) and (C) $U(D_1)$ in the θ-$\dot\theta$ plane and $(\theta+\dot\theta)$-$(\theta-\dot\theta)$ plane, respectively. (D) and (E) $D_1\cap R$ in the θ-$\dot\theta$ plane and the $(\theta+\dot\theta)$-$(\theta-\dot\theta)$ plane, respectively.

figure 3(E), the numbers of slits in D_1, D_2, and D_3 remain unchanged for γ. Therefore, we assume that the mechanism is common for γ when n is small. We used $\gamma=0.013$ to show the results below.

Since $R=S(D_1)=T(U(D_1))$, we first examine $U(D_1)$. In particular, the boundaries of $U(D_1)$ are $\theta=0, \theta=-\pi/2$, and $2\dot\theta=\dot\varphi$ from the foot contact conditions (4) and (5), as shown in figure 4(A). In addition, since D_1 does not intersect with W^{cu}, D_1 and $U(D_1)$ are on the same side with respect to W^{cu}, and $U(D_1)$ also has a boundary near W^{cu} (strictly speaking, D_1 intersects with W^{cu} in a small range of $0<\theta<\gamma$, but has no influence in the formation of $D_1\cap R$ and so is ignored). Figure 4(B) shows the result for $U(D_1)$ projected onto the θ-$\dot\theta$ plane (figure 4(C) uses $\theta+\dot\theta$ and $\theta-\dot\theta$ for the axes in order to clarify the geometric characteristics).

Since T is a one-to-one mapping for $[\theta\,\dot\theta]$, the boundaries of $U(D_1)$ on the θ-$\dot\theta$ plane become the boundaries of R by T, as shown in figure 4(A). Figure 4(D) shows the result of R obtained from (6) (figure 4(E) uses $\theta+\dot\theta$ and $\theta-\dot\theta$ for the axes to clarify the geometric characteristics). The boundaries a_1b_1 and c_1d_1 of $D_1\cap R$ are obtained by applying T to the boundaries near W^{cu} and $2\dot\theta=\dot\varphi$, respectively, of $U(D_1)$.

3.3. Characteristics of S^{-1}

Next, we investigate $D_2=S^{-1}(D_1\cap R)$. Since $S^{-1}(D_1\cap R)=U^{-1}(T^{-1}(D_1\cap R))$, we first examine $T^{-1}(D_1\cap R)$. From (6), $T^{-1}(D_1\cap R)$ is described by

$$\left\{[-\theta^+ - 2\theta^+\ \dot\theta^+\sec 2\theta^+\ \dot\varphi^-]\ \middle|\ [\theta^+\ \varphi^+\ \dot\theta^+\ \dot\varphi^+]\right.$$
$$\left.\in D_1\cap R,\ \dot\varphi^-\in\mathbb{R}\right\} \qquad (15)$$

$[\theta\,\varphi\,\dot\theta]$ in $T^{-1}(D_1\cap R)$ is uniquely determined using $D_1\cap R$ in figure 4(D). Figure 5(A) shows the result of $T^{-1}(D_1\cap R)$ in the θ-$\dot\theta$ plane. (Figure 5(B) uses $\theta+\dot\theta$ and $\theta-\dot\theta$ for the axes to clarify the geometric characteristics.) The boundary $\hat a_1\hat b_1\hat c_1\hat d_1$ of $T^{-1}(D_1\cap R)$ is obtained by applying T^{-1} to the boundary $a_1b_1c_1d_1$ of $D_1\cap R$ in figure 4(D). Note that $*_1$ and $\hat *_1$ (except for D_1), such as a_1 and $\hat a_1$, are used for $D_1\cap R$ and $T^{-1}(D_1\cap R)$, respectively. Since $T^{-1}(D_1\cap R)$

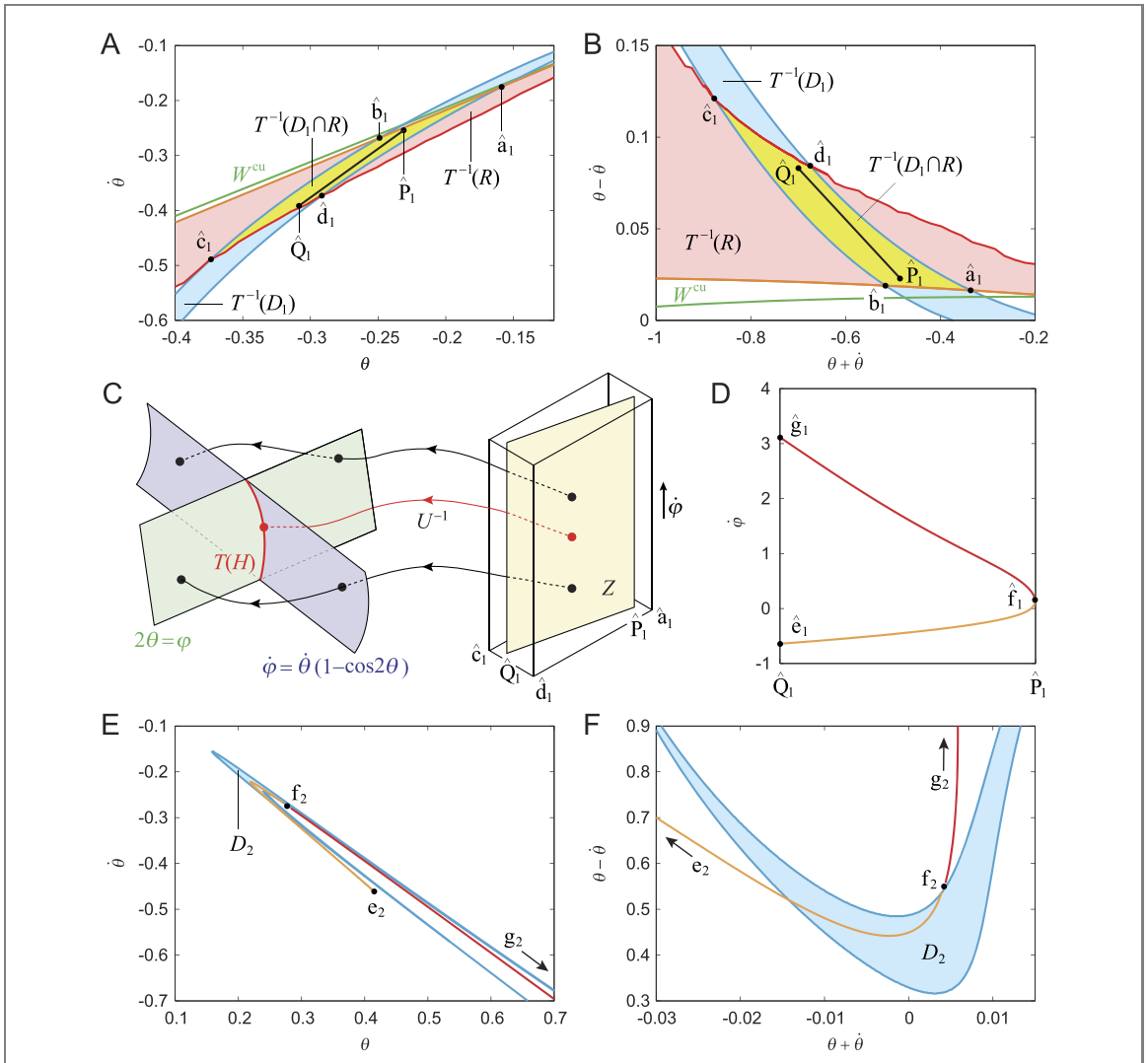

Figure 5. Characteristics of $S^{-1}(D_1 \cap R) = U^{-1}(T^{-1}(D_1 \cap R))$. (A) and (B) $T^{-1}(D_1 \cap R)$ on H in the θ-$\dot{\theta}$ plane and the $(\theta+\dot{\theta})$-$(\theta-\dot{\theta})$ plane, respectively. (C) Schematic diagram of applying U^{-1} to plane Z. (D) Curve $\hat{e}_1\hat{f}_1\hat{g}_1$ in Z to which U^{-1} is applicable. (E) and (F) Curve $e_2f_2g_2$ and D_2 in the θ-$\dot{\theta}$ plane and the $(\theta+\dot{\theta})$-$(\theta-\dot{\theta})$ plane, respectively.

is thin, as shown in figure 5(A), we extract a line segment $\hat{P}_1\hat{Q}_1$ from $T^{-1}(D_1 \cap R)$. However, since $\dot{\varphi}$ in $T^{-1}(D_1 \cap R)$ is not uniquely determined, we consider $T^{-1}(D_1 \cap R)$ as a quadrangular prism, the height of which is in the $\dot{\varphi}$ direction, as shown in figure 5(C). Then, line segment $\hat{P}_1\hat{Q}_1$ is considered to be a plane, which we call plane Z. We apply U^{-1} to the plane Z. Since U^{-1} is the map from H to $T(H)$ and $T(H)$ is a two-dimensional surface that has two constraint conditions (7) and (8) in the four-dimensional phase space, U^{-1} is applicable only to points in the plane Z that simultaneously satisfy the two conditions when the points are moved in the phase space in the time reverse direction using the equations of motion (1) and (2), as shown in figure 5(C). These points determine $\dot{\varphi}$ in $T^{-1}(D_1 \cap R)$. Figure 5(D) shows the result for the collection of the points in the plane Z indicated by the curve $\hat{e}_1\hat{f}_1\hat{g}_1$ to which U^{-1} is applicable. We obtained the curve $e_2f_2g_2$ by applying U^{-1} to this curve $\hat{e}_1\hat{f}_1\hat{g}_1$, as shown in figure 5(E). (Figure 5(F) uses $\theta+\dot{\theta}$ and $\theta-\dot{\theta}$ for the axes to clarify the geometric characteristics.) Note that $*_2$ (except for D_2), such as e_2, is used for D_2. In order to obtain the curves $e_2f_2g_2$ and $\hat{e}_1\hat{f}_1\hat{g}_1$ in figures 5(D) through (F), we linearized the equations of motion (1) and (2) for θ and φ because the walking behavior appears around the saddle $[\gamma\,0\,0\,0]$. Therefore, there are differences from the exact solution, as the approximately obtained curve $e_2f_2g_2$ is not inside D_2 (figures 5(E) and (F), see the appendix A for details). The curve $e_2f_2g_2$, specifically the curve e_2f_2 is bent to be V-shaped, as shown in figure 5(E). (Figure 5(F) uses $\theta+\dot{\theta}$ and $\theta-\dot{\theta}$ for the axes to clarify the geometric characteristics.)

In order to examine where in $D_1 \cap R$ the curve $e_2f_2g_2$ is moved from by $S^{-1}(= U^{-1} \circ T^{-1})$, we investigate where in $D_1 \cap R$ the curve $\hat{e}_1\hat{f}_1\hat{g}_1$ is moved from by T^{-1}. Since the curve $\hat{e}_1\hat{f}_1\hat{g}_1$ is in $T^{-1}(D_1 \cap R)$, the curve moves in $D_1 \cap R$ by T. Figures 4(D) and (E) show the result indicated by the curve P_1Q_1. This shows that when S^{-1} is applied to the curve P_1Q_1 in $D_1 \cap R$, two curves f_2e_2 and f_2g_2 are obtained in $T(H)$. Since $D_1 \cap R$ is thin, as shown in figure 4(D),

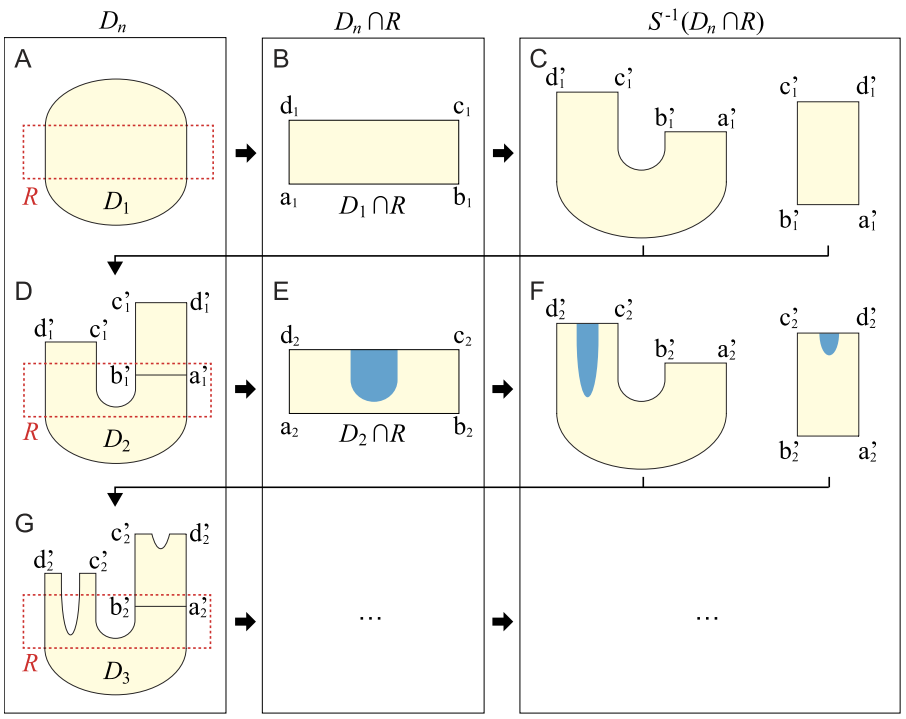

Figure 6. Schematic diagram of the process used to deform D_1 to D_2 and D_3 and generate slits. $D_1 \cap R$ is extracted from (A) in (B). Two regions are generated by S^{-1} in (C) and are connected to form D_2 in (D). In the same manner, $D_2 \cap R$ is extracted in (E). Two regions are generated by S^{-1} in (F) and are connected to form D_3 in (G).

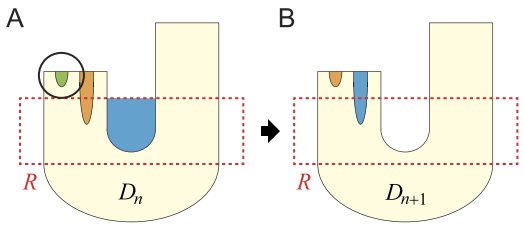

Figure 7. Unchanged number of slits. When (A) the generated slit in D_n does not reach R, (B) the number of slits remains unchanged in D_{n+1}.

the curve P_1Q_1 approximates $D_1 \cap R$. Therefore, the process to obtain the V-shaped curve $e_2f_2g_2$ from the curve P_1Q_1 explains the process by which $D_1 \cap R$ is transferred to D_2.

Figures 6(A) through (D) show a schematic diagram of the summary by which to obtain D_2 from D_1. Specifically, $D_1 \cap R$ is extracted from D_1 (figure 6(B)), and two regions are generated by S^{-1}, one of which is stretched and bent (figure 6(C) left), and the other of which is only stretched (figure 6(C) right). These regions are connected at the boundaries $a_1' b_1'$ to form D_2 (figure 6(D)).

Next, we move to $D_3 = S^{-1}(D_2 \cap R)$. Since $D_2 \subseteq D_1$, the deformation from D_2 to D_3 (figures 6(D) through (G)) is the same as that from D_1 to D_2 (figures 6(A) through (D)). Since D_2 is V-shaped (figure 6(D)), the extracted $D_2 \cap R$ is also V-shaped and has a large slit at the boundary c_2d_2 (figure 6(E)). The large slit becomes slits at the boundary $c_2' d_2'$ in D_3 by the deformation (figures 6(F) and (G)). Although figure 6(F) (right) has a slit, it is far from R and so is ignored (figure 6(G)).

When the slit generated in D_n reaches, but does not penetrate, R, one slit is added in D_{n+1}, as observed in the process from D_2 to D_3. In contrast, when the generated slit in D_n does not reach R, the number of slits in D_{n+1} remains unchanged, as shown in figure 7. Moreover, since $D_{n+1} \subseteq D_n$, it is possible that the slit becomes deeper as n increases to reach R and create a new slit. Therefore, when the generated slit in D_n does not penetrate R, the number of slits of D_{n+1} increases by one or remains unchanged.

3.4. Appearance of a fractal

We consider the cases in which the generated slit in D_n penetrates R for the first time at $n = N$, as shown in figure 8(A). (There may be multiple slits that do not penetrate $D_N \cap R$ to the left and right of the generated slit, but because they do not affect the explanation below, they are not shown in figure 8.) By applying S^{-1} to D_N in the same manner as in figure 6, a penetrating slit appears close to the outer edge of the V-shaped D_{N+1}, as shown in figure 8(D). In addition, since $D_{n+1} \subseteq D_n$ once a slit penetrates R, the slit penetrates R for $n > N$. Furthermore, the penetrating slit close to the outer edge of D_{N+1} generates a slit that penetrates R near the right edge of $D_{N+1} \cap R$, as shown in figure 8(E). As a result, a penetrating slit also appears close to the inner edge of the V-shaped D_{N+2}, as shown in figure 8(G). Furthermore,

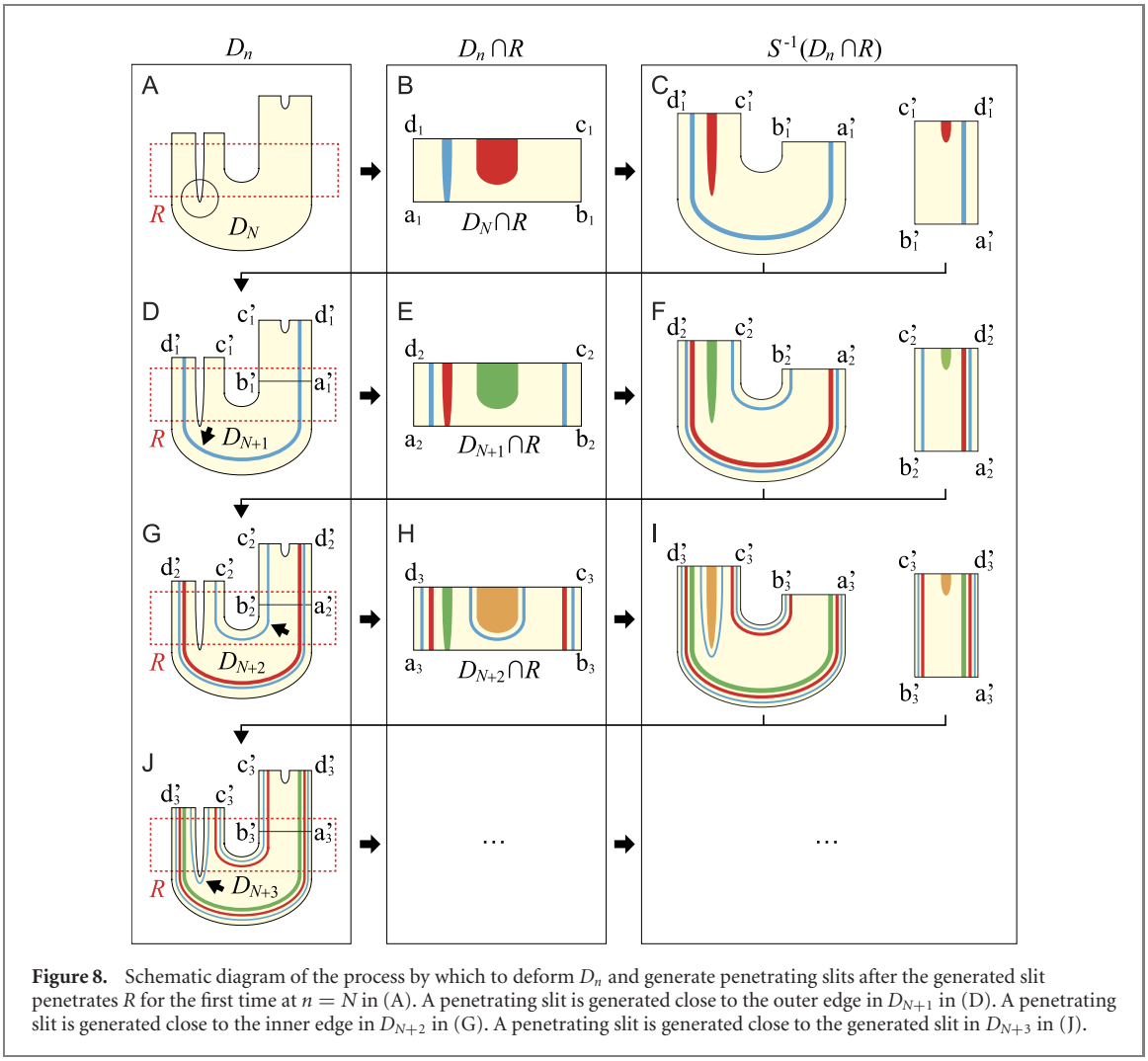

Figure 8. Schematic diagram of the process by which to deform D_n and generate penetrating slits after the generated slit penetrates R for the first time at $n = N$ in (A). A penetrating slit is generated close to the outer edge in D_{N+1} in (D). A penetrating slit is generated close to the inner edge in D_{N+2} in (G). A penetrating slit is generated close to the generated slit in D_{N+3} in (J).

the penetrating slit produces another penetrating slit in D_{N+3} near the slit generated by the large slit of D_{N+2} due to the V-shape, as shown in figure 8(J). This slit also penetrates R. These penetrating slits produce new penetrating slits near the edge, and the number of slits increases at an accelerated rate as n increases. As a result, a fractal basin of attraction appears.

Figures 9(A) through (E) show D_4 to D_8 for $\gamma = 0.013$. At $N = 5$, the generated slit penetrated R for the first time (figure 9(B)). After that, the penetrating slits were generated close to the outer edge at $n = 6$ (figure 9(C)), near the inner edge at $n = 7$ (figure 9(D)), and close to the generated slit at $n = 8$ (figure 9(E)) in that order. Therefore, infinitely many slits are generated and the fractal basin of attraction appears, as shown in figures 3(C) and (D).

3.5. No fractal appears

Next, we consider the cases in which no slits in D_n penetrate R, even when S^{-1} is applied several times. In particular, suppose that n is so large that D_n converges and also suppose that D_n has a slit that does not reach R. In this case, since the number of slits does not change even when S^{-1} is applied, the basin of attraction does not have a fractal structure and has a finite number of slits.

Figures 10(A) and (B) show D_{50} and D_{51}, respectively, for $\gamma = 0.001$. Here, D_{50} has four slits, and the leftmost slit does not reach R. As a result, D_{51} has four slits as in D_{50}. In addition, D_{50} and D_{51} have no difference and are identical to the basin of attraction (figure 3(B)), which we confirmed by comparing the regions using $10^4 \times 10^4$ initial states, and so converge. Therefore, the basin of attraction does not have a fractal structure.

4. Discussion

4.1. Stability and basin of attraction

Bipedal walking has intrinsic instability due to saddle dynamics, and clarifying the mechanism by which walking can be stabilized is important. Passive dynamic walking is a useful model to examine the mechanism from a dynamic viewpoint. In order to clarify the stabilization mechanism, investigating both the stability and basin of attraction is crucial. However, while previous studies have focused on the stability by the eigenvalue analysis of the linearized Poincaré map around the fixed point on the

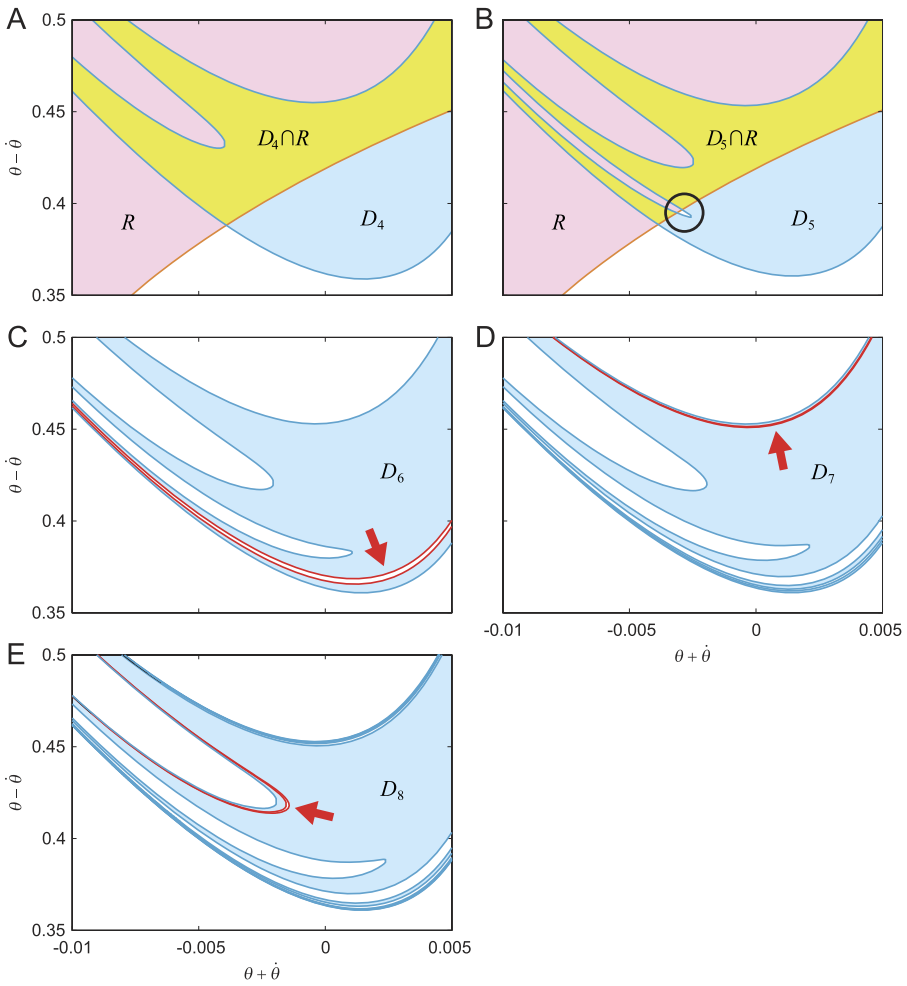

Figure 9. D_4 to D_8 for $\gamma = 0.013$. (A) No slit penetrates R. (B) The generated slit penetrates R for the first time. (C) A penetrating slit is generated close to the outer edge of D_6. (D) A penetrating slit is generated close to the inner edge of D_7. (E) A penetrating slit is generated close to the generated slit of D_8.

Poincaré section [8, 13, 15, 16, 21, 35–37], the basin of attraction has not been well studied. This is partly because while eigenvalue analysis allows us to easily investigate the stability, no general analytical method has been provided for investigating the basin of attraction. We used an analytical approach based on dynamical systems theory to clarify a specific property embedded in the basin of attraction, which is useful to further investigate the characteristics of the basin of attraction in walking. While passive dynamic walking has no control or input, the use of control and input changes the dynamic characteristics of walking and also varies the stability and the basin of attraction [3, 4, 30, 31, 34]. We would like to improve and clarify our analysis in the future.

4.2. Initial-value sensitivity and convergence to attractor

The Poincaré map S represents walking one step, and slits are generated by applying the inverse image S^{-1} many times to the region from which the model walks at least one step. These slits come from the large slit of the V-shaped D_2 (figure 6). When there are only a finite number of slits in the basin of attraction, the generated slit in D_n does not reach R and is not used in D_{n+1} (figure 7). Therefore, these slits are not stretched much. In contrast, once the generated slit in D_n penetrates R, the generated slits for $n \geqslant N$ are stretched greatly and create stripe patterns by producing penetrating slits, especially close to the basin boundary (figure 8). These penetrating slits become thinner as n increases. Since slits indicate a region in which the model will fall down, whether the model continues to walk or not becomes very sensitive around the basin boundary. Furthermore, since penetrating slits become thinner, two states located at different sides of the large slit of D_2 become closer as S^{-1} is applied to the two states many times. This means that two states located at different sides of a thin slit in the basin of attraction move away from each other as S is applied many times and the two states come to reach different sides of the large slit of D_2.

When the basin of attraction is fractal, there are infinitely many penetrating slits close to the basin boundary. Therefore, when the model walks from an initial state near the boundary on the basin of

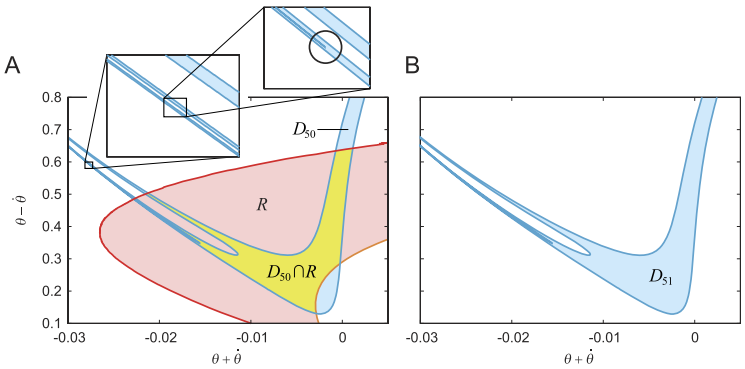

Figure 10. No appearance of fractal. (A) and (B) D_{50} and D_{51}, respectively, for $\gamma = 0.001$. The generated slit in D_{50} does not reach R. D_{50} and D_{51} have the same shape and converge. The number of slits never increases.

attraction, there are numerous penetrating slits between the initial state and the attractor, and the model must traverse the slits for the state to approach the attractor. The model must walk at least the steps that are required to generate the penetrating slits by applying S^{-1}. Therefore, the model takes a long time to approach the attractor, depending on the initial state.

4.3. Limitations of our analysis

In the present study, we clarified that the fractal basin of attraction appears when the generated slit in D_n penetrates R and that fractal basin of attraction does not appear when the generated slit in D_n does not reach R for an n so large that D_n converges. However, it is possible that the generated slit in D_n reaches, but does not penetrate, R for so large n that D_n converges. In this case, although it is not at an accelerated rate, the number of slits increases as n increases. While infinitely many slits appear in the basin of attraction, no penetrating slits are generated. Although our analysis does not exclude this possibility, our simulation results did not show such a case for any γ.

We used the simplest walking model for the analysis of passive dynamic walking, i.e., we assumed the extreme case $m/M \to 0$ and $b/l \to 1$ for the compass-type model [13]. Therefore, we did not explain the mechanism of the basin of attraction for general models of passive dynamic walking. However, the period-doubling cascade to chaos appears and the fractal basin of attraction is observed without the period doubling even when the extreme case is not assumed [2]. This suggests that similar mechanisms to those observed herein are embedded in general models of passive dynamic walking.

4.4. Biological relevance

The fractal appears in human walking, especially in the gait rhythm [17–20]. However, unlike passive dynamic walking, human walking is generated through the control. The basin of attraction of compass-type models used in passive dynamic walking is enlarged by the control and the number of slit changes [30, 31, 34]. However, the stance leg during human walking is almost straight and rotates around the foot contact point like an inverted pendulum [28]. In addition, the stance and swing legs are switched by the foot contact and lift off. Therefore, saddle instability and hybrid properties are inevitable in the gait dynamics, as in passive dynamic walking, and the stretching and bending deformation remains crucial for the formation mechanism of basin of attraction. In fact, our previous study [30, 31] showed that even when a controller inspired by spinal central pattern generators [32] is incorporated in a compass-type model, the basin of attraction has slits due to the deformation.

Human walking is generated through the central nervous system and the body mechanical system. Fractal properties are reduced by aging and pathological disorders such as Parkinson's and Huntington's diseases [17, 20]. A simple neuromechanical model demonstrated that fractal properties are reduced by changing the motor control model to emulate the pathological disorder [12]. These properties suggest that the neural system contributes to the fractal in human walking. In contrast, the body mechanical system also has potential to contribute to the fractal in human walking. Passive dynamic walking exhibits a chaos attractor depending on the model parameter [13, 15] and shows a fractal basin of attraction even for the single attractor as shown in the present study. The steady state of a dynamical system with a single attractor never shows a fractal, but instead shows regular behavior, unless the system is disturbed. However, when the dynamical system is specific and has a fractal basin of attraction, fractal behavior can be induced by a disturbance or noise without fractal properties. In fact, the fractal appears in walking of compass-type models with a controller and noise without fractal properties [1, 14]. Even for passive dynamic walking, the mechanisms for fractal and non-fractal basins of attraction clarified in the

present study will provide useful insights for understanding human walking. The analysis of measured human data has limitations for elucidating the underlying mechanism in human walking, and physical models are useful to overcome the limitations.

Competing interests

The authors have no conflicting financial interests.

Author contributions

SA developed the study design. KO performed computer simulations and analyzed the data in consultation with SA, IO, HK, and KT KO and SA wrote the manuscript, which was reviewed and approved by all of the authors.

Acknowledgments

The present study was supported in part by JSPS KAKENHI Grant Numbers JP15KT0015 and JP17H04914.

Appendix A

A 1. Deformation of $T^{-1}(D_1 \cap R)$ by U^{-1}

Here, we approximately solve the deformation of $T^{-1}(D_1 \cap R)$ by U^{-1} based on the analysis in our previous study [29]. We first denote the solution of equations of motion (1) and (2) by $\Theta(t) = [\theta(t)\,\dot{\theta}(t)\,\varphi(t)\,\dot{\varphi}(t)]$. From the definition of U, for a point $\Theta(0) \in T^{-1}(D_1 \cap R) \subset H$, there exists $\Delta > 0$ such that

$$\Theta(-\Delta) = U^{-1}(\Theta(0)) \in T(H) \tag{16}$$

where $-\Delta$ is used as the negative time to analyze U^{-1} (figure 2(A)). $\Theta(0)$, $\Theta(-\Delta)$, and $-\Delta$ correspond to the state just before foot contact, the state just after foot contact, and the duration of a step, respectively. $\Theta(-\Delta)$ gives the deformation of $T^{-1}(D_1 \cap R)$ by U^{-1}.

Since $\Theta(-\Delta)$ is in $T(H)$, the following equations are satisfied from (7)–(9):

$$2\theta(-\Delta) = \varphi(-\Delta) \tag{17}$$

$$\dot{\varphi}(-\Delta) = \dot{\theta}(-\Delta)(1 - \cos 2\theta(-\Delta)) \tag{18}$$

$$\theta(-\Delta) > 0 \tag{19}$$

In addition, since $\Theta(-\Delta)$ is in H, the following equation is satisfied from (3):

$$2\theta(0) = \varphi(0) \tag{20}$$

In order to approximately solve (16), we linearize the equations of motion (1) and (2) around $[\gamma\ 0\ 0\ 0]$ by

$$\ddot{\theta} = \theta - \gamma \tag{21}$$

$$\ddot{\varphi} = -(\varphi - \theta + \gamma) \tag{22}$$

The solution is obtained by

$$\theta = \gamma + C_1 \exp(t) + C_2 \exp(-t) \tag{23}$$

$$\varphi - \frac{\theta - \gamma}{2} = K \cos(t + \phi) \tag{24}$$

where C_1, C_2, K, and ϕ are the integration constants ($0 \leqslant \phi < 2\pi$). Here, $\dot{\psi}$ on plane Z is obtained by

$$\dot{\varphi}(0) = \frac{C_1 - C_2}{2} - K \sin\phi \tag{25}$$

C_1 and C_2 are determined by the initial conditions of θ and $\dot{\theta}$, as follows:

$$C_1 = \frac{\theta(0) - \gamma + \dot{\theta}(0)}{2}$$

$$C_2 = \frac{\theta(0) - \gamma - \dot{\theta}(0)}{2} \tag{26}$$

In contrast, K and ϕ are determined by the initial conditions of θ, φ, $\dot{\theta}$, and $\dot{\varphi}$.

From (17), (18), (20), (23), and (24), we have the following equations:

$$\theta(-\Delta) = C_1 \exp(-\Delta) + C_2 \exp\Delta + \gamma \tag{27}$$

$$\dot{\theta}(-\Delta) = C_1 \exp(-\Delta) - C_2 \exp\Delta \tag{28}$$

$$K \cos(-\Delta + \phi) = \frac{3\theta(-\Delta)}{2} + \frac{\gamma}{2} \tag{29}$$

$$K \sin(-\Delta + \phi) = -\dot{\theta}(-\Delta)\left\{\frac{1}{2} - \cos 2\theta(-\Delta)\right\} \tag{30}$$

$$K \cos\phi = \frac{3}{2}\left(C_1 + C_2 + \frac{4\gamma}{3}\right) \tag{31}$$

where Δ, ϕ, K, $\theta(-\Delta)$, and $\dot{\theta}(-\Delta)$ are unknown variables (C_1 and C_2 are determined in (26) from $[\theta(0)\,\dot{\theta}(0)]$). We obtain $\Theta(-\Delta)$ from $[\theta(0)\,\dot{\theta}(0)]$ by solving (27)–(31).

In order to show how U^{-1} deforms $T^{-1}(D_1 \cap R)$, we used the approximated solution given above. In particular, we used the line segment $\hat{P}_1\hat{Q}_1$ within $T^{-1}(D_1 \cap R)$, as shown figure 5(A) ($\hat{P}_1$: $[\theta\,\dot{\theta}] = [-0.2311\ -0.2536]$, $\hat{Q}_1$: $[\theta\,\dot{\theta}] = [-0.3085\ -0.3915]$). This segment was moved to two curves f_2e_2 and f_2g_2 by U^{-1}, which approximate $U^{-1}(T^{-1}(D_1 \cap R))$, as shown in figure 5(E).

ORCID iDs

Shinya Aoi https://orcid.org/0000-0001-9243-2641

References

[1] Ahn J and Hogan N 2013 Long-range correlations in stride intervals may emerge from non-chaotic walking dynamics *PloS One* **8** e73239

[2] Akashi N, Nakajima K and Kuniyoshi Y 2019 Unpredictable as a dice: analyzing riddled basin structures in passive dynamic walker *Proc. Int. Symp. Micro-NanoMechatron. Human Sci.* pp 119–23

[3] Aoi S and Tsuchiya K 2006 Stability analysis of a simple walking model driven by an oscillator with a phase reset using sensory feedback *IEEE Trans. Robot.* **22** 391–7

[4] Aoi S and Tsuchiya K 2007 Self-stability of a simple walking model driven by a rhythmic signal *Nonlinear Dyn.* **48** 1–16

[5] Asano F, Luo Z-W and Yamakita M 2005 Biped gait generation and control based on a unified property of passive dynamic walking *IEEE Trans. Robot.* **21** 754–62

[6] Bruijn S M, Bregman D J J, Meijer O G, Beek P J and van Dieën J H 2011 The validity of stability measures: a modelling approach *J. Biomech.* **44** 2401–8

[7] Chyou T, Liddell G F and Paulin M G 2011 An upper-body can improve the stability and efficiency of passive dynamic walking *J. Theor. Biol.* **285** 126–35

[8] Coleman M J and Ruina A 1998 An uncontrolled walking toy that cannot stand still *Phys. Rev. Lett.* **80** 3658–61

[9] Collins S, Ruina A, Tedrake R and Wisse M 2005 Efficient bipedal robots based on passive dynamic walkers *Science* **307** 1082–5

[10] Collins S H, Wisse M and Ruina A 2001 A three-dimensional passive-dynamic walking robot with two legs and knees *Int. J. Robot. Res.* **20** 607–15

[11] Donelan J M, Kram R and Kuo A D 2002 Mechanical work for step-to-step transitions is a major determinant of the metabolic cost of human walking *J. Exp. Biol.* **205** 3717–27

[12] Fu C, Suzuki Y, Morasso P and Nomura T 2020 Phase resetting and intermittent control at the edge of stability in a simple biped model generates 1/*f*-like gait cycle variability *Biol. Cybern.* **114** 95–111

[13] Garcia M, Chatterjee A, Ruina A and Coleman M 1998 The simplest walking model: stability, complexity, and scaling *ASME J. Biomech. Eng.* **120** 281–8

[14] Gates D H, Su J L and Dingwell J B 2007 Possible biomechanical origins of the long-range correlations in stride intervals of walking *Physica* A **380** 259–70

[15] Goswami A, Thuilot B and Espiau B 1998 A study of the passive gait of a compass-like biped robot: symmetry and chaos *Int. J. Robot. Res.* **17** 1282–301

[16] Gritli H, Khraief N and Belghith S 2012 Period-three route to chaos induced by a cyclic-fold bifurcation in passive dynamic walking of a compass-gait biped robot *Commun. Nonlinear Sci. Numer. Simulat.* **17** 4356–72

[17] Goldberger A L, Amaral L A N, Hausdorff J M, Ivanov P C, Peng C-K and Stanley H E 2002 Fractal dynamics in physiology: alterations with disease and aging *Proc. Natl Acad. Sci. USA* **99** 2466–72

[18] Hausdorff J M, Peng C K, Ladin Z, Wei J Y and Goldberger A L 1995 Is walking a random walk? Evidence for long-range correlations in stride interval of human gait *J. Appl. Physiol.* **78** 349–58

[19] Hausdorff J M, Purdon P L, Peng C K, Ladin Z, Wei J Y and Goldberger A L 1996 Fractal dynamics of human gait: stability of long-range correlations in stride interval fluctuations *J. Appl. Physiol.* **80** 1448–57

[20] Hausdorff J M, Mitchell S L, Firtion R, Peng C K, Cudkowicz M E, Wei J Y and Goldberger A L 1997 Altered fractal dynamics of gait: reduced stride-interval correlations with aging and Huntington's disease *J. Appl. Physiol.* **82** 262–9

[21] Hobbelen D G E and Wisse M 2008 Swing-leg retraction for limit cycle walkers improves disturbance rejection *IEEE Trans. Robot.* **24** 377–89

[22] Hosoda K, Takuma T, Nakamoto A and Hayashi S 2008 Biped robot design powered by antagonistic pneumatic actuators for multi-modal locomotion *Robot. Auton. Syst.* **56** 46–53

[23] Kinugasa T, Ito T, Kitamura H, Ando K, Fujimoto S, Yoshida K and Iribe M 2015 3D dynamic biped walker with flat feet and ankle springs: passive gait analysis and extension to active walking *J. Robot. Mechatron.* **27** 444–52

[24] Kuo A D 2001 A simple model of bipedal walking predicts the preferred speed-step length relationship *ASME J. Biomech. Eng.* **123** 264–9

[25] Kuo A D 2001 Energetics of actively powered locomotion using the simplest walking model *ASME J. Biomech. Eng.* **124** 113–20

[26] Kuo A D, Donelan J M and Ruina A 2005 Energetic consequences of walking like an inverted pendulum: step-to-step transitions *Exerc. Sport Sci. Rev.* **33** 88–97

[27] McGeer T 1990 Passive dynamic walking *Int. J. Robot. Res.* **9** 62–82

[28] Mochon S and McMahon T A 1980 Ballistic walking *J. Biomech.* **13** 49–57

[29] Obayashi I, Aoi S, Tsuchiya K and Kokubu H 2016 Formation mechanism of a basin of attraction for passive dynamic walking induced by intrinsic hyperbolicity *Proc. R. Soc.* A **472** 20160028

[30] Obayashi I, Aoi S, Tsuchiya K and Kokubu H 2015 Common formation mechanism of basin of attraction for bipedal walking models by saddle hyperbolicity and hybrid dynamics *Japan J. Ind. Appl. Math.* **32** 315–32

[31] Okamoto K, Aoi S, Obayashi I, Kokubu H, Senda K and Tsuchiya K 2019 Investigating phase resetting effect on basin of attraction for walking using a simple model *Proc. Int. Symp. Adapt. Motion Anim. Mach.*

[32] Orlovsky G N, Deliagina T and Grillner S 1999 *Neuronal Control of Locomotion: from Mollusc to Man* (Oxford: Oxford University Press)

[33] Schwab A L and Wisse M 2001 Basin of attraction of the simplest walking model *Proc. ASME Design Eng. Tech. Conf.* pp 9–12

[34] Sidorov E and Zacksenhouse M 2019 Lyapunov based estimation of the basin of attraction of Poincare maps with applications to limit cycle walking *Nonlinear Anal. Hybrid Syst.* **33** 179–94

[35] Sugimoto Y and Osuka K 2008 Hierarchical implicit feedback structure in passive dynamic walking *J. Robot. Mechatron.* **20** 559–66

[36] Wisse M, Schwab A L, van der Linde R Q and van der Helm F C T 2005 How to keep from falling forward: elementary swing leg action for passive dynamic walkers *IEEE Trans. Robot.* **21** 393–401

[37] Wisse M, Hobbelen D G E and Schwab A L 2007 Adding the upper body to passive dynamic walking robots by means of a bisecting hip mechanism *IEEE Trans. Robot.* **23** 112–23